ATLAS NOTE

ATLAS-CONF-2011-112

July 29, 2011

Combined Standard Model Higgs Boson Searches in pp Collisions at $\sqrt{s} = 7$ TeV with the ATLAS Experiment at the LHC

The ATLAS collaboration

Abstract

A combination of searches for the Standard Model Higgs boson by the ATLAS experiment at the LHC is presented. This combination uses a dataset corresponding to an integrated luminosity ranging from 1.04 to 1.21 fb^{-1} of pp collisions at a centre-of-mass energy of 7 TeV. It updates the combination of previous searches in the channels $H \to \gamma\gamma$, $H \to WW^{(*)} \to \ell\nu\ell\nu$, $H \to WW \to \ell\nu qq$, $H \to ZZ^{(*)} \to \ell\ell\ell\ell$, $H \to ZZ \to \ell\ell\nu\nu$ and $H \to ZZ \to \ell\ell qq$ and includes searches for $WH \to \ell\nu b\bar{b}$ and $ZH \to \ell\ell b\bar{b}$ for the first time. No significant evidence for a signal is observed. The Higgs boson mass ranges 155 GeV to 190 GeV and 295 GeV to 450 GeV are excluded at the 95% CL, which is similar to the expected exclusion mass ranges in the absence of a signal of 136 GeV to 196 GeV and 327 GeV to 443 GeV. In the low mass range ($\sim 120 - 140$ GeV) an excess of events with a significance of approximately 2.8σ above the background expectation is observed.

1 Introduction

Thanks to the excellent operation of the Large Hadron Collider (LHC) in 2011, the amount of data delivered has exceeded expectations. By the end of June, data corresponding to an integrated luminosity of 1.23 fb^{-1} at $\sqrt{s}$ =7 TeV had been recorded by the ATLAS experiment. With this data set several channels are beginning to be sensitive to a Standard Model Higgs boson [1–6]. To provide the most powerful results in the search for the Higgs boson, individual channels need to be statistically combined. The results of that combination are presented in this note.

Prior to the LHC, the best direct information on the mass of the Standard Model Higgs boson was a lower limit of 114.4 GeV at the 95% confidence level, set using the combined results of the four LEP experiments [7] and an excluded band of 158 GeV to 173 GeV from the combined Tevatron experiments [8, 9].

All the channels which were combined for the data collected in 2010 [10] (*i.e.* the $H \to \gamma\gamma$, $H \to WW^{(*)} \to \ell\nu\ell\nu$, $H \to ZZ^{(*)} \to \ell\ell\ell\ell$, $H \to WW \to \ell\nu qq$, $H \to ZZ \to \ell\ell\nu\nu$, and $H \to ZZ \to \ell\ell qq$) have been updated [11–16] and are used again herein. Significant improvements in the analyses with respect to the combination published in Ref. [10] occurred in the $H \to \gamma\gamma$ and $H \to ZZ \to \ell\ell qq$ channels. In both cases the sensitivity has been enhanced by separating events into independent categories of uneven sensitivities instead of treating all events inclusively. New analyses with a reduced sensitivity with respect to the aforementioned ones, that search for WH and ZH production, followed by the $H \to b\bar{b}$ decay, are considered for the first time.

The data used in the various combination channels were collected in 2011 predominantly with one LHC bunch pattern corresponding to a 50 ns bunch spacing[1]. The increase of data delivered by the LHC came at the cost of an average number of interactions per bunch crossing of up to $\sim$8 at the start of LHC fills. This change in event environment with respect to the data taken in 2010 required in-depth studies of the impact of additional inelastic scattering events occurring both in and out-of-time with respect to the hard scattering process of interest. These effects are included in the ATLAS Monte Carlo simulation. Their impact on all the search channels presented in this note has been studied and taken into account and has in most cases led to a modest re-optimisation of the selection criteria to mitigate the effects.

2 The ATLAS detector and data sample

The ATLAS detector [17] is a multipurpose particle physics apparatus with a forward-backward symmetric cylindrical geometry and near 4π coverage in solid angle[2]. The overall layout of the detector is dominated by its four superconducting magnet systems, which comprise a thin solenoid surrounding inner tracking detectors and three large toroids with an eightfold azimuthal symmetry.

The inner detector provides precision tracking for charged particles in the pseudorapidity range $|\eta| < 2.5$. It consists of silicon pixel and strip detectors surrounded by a straw tube tracker that also provides transition radiation measurements for electron identification. The calorimeter system covers the pseudorapidity range $|\eta| < 4.9$. For $|\eta| < 3.2$, high-granularity liquid-argon (LAr) electromagnetic sampling calorimeters are used. An iron-scintillator tile calorimeter provides hadronic coverage in the range $|\eta| < 1.7$. The end-cap and forward regions, spanning $1.5 < |\eta| < 4.9$, use LAr calorimeters for both electromagnetic and hadronic measurements. The muon spectrometer has separate trigger and high-precision tracking chambers covering $|\eta| < 2.7$.

[1]A very small amount ($\sim$ 1.4%) of the data were recorded with an inter-bunch spacing of 75 ns. This has a very small impact on the results.

[2]ATLAS uses a right-handed coordinate system with its origin at the nominal interaction point (IP) in the centre of the detector and the z-axis along the beam pipe. The x-axis points from the IP to the centre of the LHC ring, and the y-axis points upward. Cylindrical coordinates (r, ϕ) are used in the transverse plane, ϕ being the azimuthal angle around the beam pipe. The pseudorapidity is defined in terms of the polar angle θ as $\eta = -\ln\tan(\theta/2)$.

A three-level trigger system selects events to record for offline analysis. Candidate events are selected using unprescaled combinations of electron, muon and photon triggers with thresholds typically 18 GeV to 20 GeV. Data are only used if all the subsystems required for a particular analysis are fully operational. Applying this requirement to pp collision data taken at a centre-of-mass energy of $\sqrt{s} = 7$ TeV with stable beam conditions results in data samples with a time-integrated luminosity between $1.04\,\mathrm{fb}^{-1}$ and $1.21\,\mathrm{fb}^{-1}$ depending on the search channel.

3 Search Channels

All search channels are described in detail in their respective references. Only the features relevant to the combination, such as the background estimation methods, the discriminating variables considered and the systematic uncertainties are recalled here. For all relevant channels, a lepton ℓ denotes an electron or a muon. The numbers of observed events and expected signal and background events are summarized in Table 1. To illustrate the relative strength of each channel these numbers of events are given in an interval containing $\sim 90\%$ of the signal around the most probable value of the invariant or transverse mass distributions, except for the $H \to WW^{(*)} \to \ell\nu\ell\nu$ channels, where the window defined in the analysis is used. In every case the fit performed uses more information than is presented here, the precise sensitivity of the analyses can therefore not be deduced from these numbers.

- $H \to \gamma\gamma$: This analysis is carried out for Higgs boson mass hypotheses between 110 GeV and 150 GeV and uses an integrated luminosity of 1.08 fb^{-1} [11]. The diphoton channel has been improved with respect to the published analysis [10], by separating the selected events into five independent categories based on the direction in which each photon was emitted (and hence the detector resolution and different signal-to-background ratio) and its photon to electron-pair conversion status (*i.e.* whether or not it is reconstructed as a conversion). These categories are treated as independent channels with fully correlated systematic uncertainties. The background is estimated from a combined signal and background fit to the diphoton invariant mass spectrum, which is the sole discriminant used in the definition of the test statistic. The invariant mass distribution of the observed candidates, summing over categories, can be seen in Fig. 1(a).

- $H \to ZZ^{(*)} \to \ell\ell\ell\ell$: The search for the Higgs boson decaying into $\ell^+\ell^-\ell^+\ell^-$, often referred to as the golden channel of Higgs boson searches at the LHC due to its good invariant mass resolution and clean signature, is described in detail in Ref. [14]. Results are given for Higgs boson mass hypotheses in the 110 GeV to 600 GeV range and using data corresponding to integrated luminosities of 1.07 to 1.21 fb^{-1} for the channels with electrons and for the four-muon channel, respectively. The lowest transverse momentum requirement on electrons has been lowered to 7 GeV, compared to the analysis published in Ref. [10], thus matching that of the muon, to improve the sensitivity to a light Higgs boson. Another important difference is that the main irreducible $ZZ^{(*)}$ background is now estimated with the MCFM V6 program [18]. All detector and luminosity related systematic uncertainties are taken to be fully correlated between signal and background. The reducible Z+jets and top-quark backgrounds, which have a larger impact in the low invariant mass range, are estimated from data control regions. The invariant mass distribution of the selected events after all cuts is given in Fig. 1(b). There is a total of two four-electron events, ten four-muon events, and six mixed, to be compared with 2.6, 5.4 and 6.6 expected background events.

- $H \to b\bar{b}$: The WH ($\ell\nu b\bar{b}$) and ZH ($\ell^+\ell^- b\bar{b}$) analyses search for the Higgs boson in the mass range between 110 GeV and 130 GeV. These searches are based on data corresponding to an integrated luminosity of 1.04 fb^{-1}. After identifying the vector boson through its leptonic decay, events are examined for the presence of two b-tagged jets. Higgs boson candidates are searched for by looking for an excess in the invariant mass distribution of the two b-tagged jets ($m_{b\bar{b}}$). The analyses are described in detail in Ref. [19].

In the $\ell\nu b\bar{b}$ channel, the dominant backgrounds arise from top-quark production and W+jets. The top background is significantly reduced by requiring exactly two jets. The remaining contribution from top and W+jets backgrounds is determined by a simultaneous template fit to the $m_{b\bar{b}}$ distribution in the signal-free control regions of $m_{b\bar{b}} < 80$ GeV, where W+jets dominates, and $140 < m_{b\bar{b}} < 250$ GeV which is dominated by top background. The small contribution from other backgrounds is subtracted from the $m_{b\bar{b}}$ distribution before the fit. The top and W+jets templates are determined from Monte Carlo simulation for $t\bar{t}$ events and un-tagged W+jets events from data. Only the normalization of the templates is left free to vary in the fit. The systematic uncertainties on the top and W+jets backgrounds were estimated to be $\pm6\%$ and $\pm14\%$, respectively, from the statistical uncertainty in the sideband fit. Relaxing the two-jet requirement to three jets provides a control sample dominated by top-pair production which is used to check its shape and normalization. Both were found to be well described. Finally, the multi-jet background, which contributes noticeably in this channel, is also determined by fitting to a template obtained by reversing cuts on the lepton isolation. Due to the limited number of simulated events, a systematic uncertainty of 50% is assigned to this background. The invariant mass distribution of the $b\bar{b}$ pairs of the selected candidates is shown Fig. 1(c).

In the $\ell^+\ell^- b\bar{b}$ channel the requirement for the two electrons or muons to be consistent with a Z boson decay improves the purity and partially compensates for the lower signal cross section. The dominant background comes from Z+jets production. Its normalization is estimated in a control sample in the sidebands defined by $m_{b\bar{b}} < 80$ GeV and $140 < m_{b\bar{b}} < 250$ GeV and its shape is taken from the Monte Carlo simulation. A systematic uncertainty of $\pm11\%$ is assigned to this background, based on the statistical uncertainty of the method. An additional small uncertainty is assigned to the shape of the $m_{b\bar{b}}$ contribution from this background, which is estimated with the use of different Monte Carlo generators. Other sources of background, among which the most relevant are top and diboson production, are estimated by Monte Carlo simulation. The background coming from top was also checked in the sidebands of the dilepton invariant mass distribution. The invariant mass distribution of the $b\bar{b}$ pairs of the selected candidates is shown Fig. 1(d).

- $H \to WW^{(*)} \to \ell\nu\ell\nu$: This search, described in detail in Ref. [12], is performed as a counting analysis for Higgs boson mass hypotheses between 110 GeV and 240 GeV, with an event selection similar to that of Ref. [10] and using an integrated luminosity of 1.04 fb^{-1}. The main background contributions are estimated from the data using control regions. The analysis is separated in 0- and 1-jet channels (the two or more jets channel is not included in this combination). To suppress the background from top-quark production in the 1-jet channel, events are rejected if the jet is tagged as a b-quark jet.

  The main background contributions stem from WW and top-quark production. The first background is measured in a control region defined essentially by a cut on the dilepton invariant mass $m_{\ell\ell}$, requiring it to exceed 80 GeV. The second background is estimated from control regions where the b-jet veto is reversed and the kinematic selection is relaxed. For the top control region in the 0-jet channel the jet veto is also removed. The relative fractions of the background contributions expected in the control and signal regions are taken from Monte Carlo simulation. The systematic uncertainty on the WW background estimate, which is mainly due to the limited control sample statistics and to the uncertainty on the extrapolation from theoretical scale variations and jet energy scale uncertainties, amounts to $\pm7.3\%$ in the 0-jet channel and $\pm14.7\%$ in the 1-jet channel. The systematic uncertainty in the estimate of the top-quark background amounts to $\pm40\%$ in the 0-jet channel and $^{+62}_{-35}\%$ in the 1-jet channel (the latter is mostly due to the uncertainty on the b-tagging efficiency). The other backgrounds such as W+jets, Z/γ^*+jets, albeit significantly smaller, are also measured in control samples of data. The small WZ and ZZ backgrounds are taken from Monte Carlo simulation. The transverse mass distributions of the candidates in the 0-jet and 1-jet channels are displayed in Figs. 1(e) and 1(f), respectively.

- $H \to WW \to \ell\nu qq$: This analysis, described in detail in Ref. [13], covers Higgs boson mass hypotheses in the 240 GeV to 600 GeV range and was carried out using data corresponding to an integrated luminosity of 1.04 fb^{-1}. This channel is also separated into 0-jet and 1-jet categories, *i.e.* zero and one jet in addition to the two jets from the W decay. A b-jet veto is applied in the 1-jet channel. The background originates overwhelmingly from the W+jets process. Using the W mass constraint on the leptonic W decay allows good reconstruction of the invariant mass of the WW system. The resolution is sufficient to directly fit the background normalization from the data with a double exponential model, similar to the approach used in the $H \to \gamma\gamma$ channel. The invariant mass distribution of the selected candidates is illustrated in Fig. 2(a).

- $H \to ZZ \to \ell\ell\nu\nu$: The analysis in this channel, described in detail in Ref. [15], has been slightly re-optimised with respect to Ref. [10]. It is carried out in the 200 GeV to 600 GeV range of Higgs boson mass hypotheses using data corresponding to an integrated luminosity of 1.04 fb^{-1}. There are two search regions, with 280 GeV and upwards considered to be *high mass*. The event selection is protected from a potential overlap with the $H \to WW^{(*)} \to \ell\nu\ell\nu$ channel by selecting events for which the invariant mass of the dilepton system is consistent with the Z boson mass. These events are specifically excluded in the $H \to WW^{(*)} \to \ell\nu\ell\nu$ analysis. The main irreducible background in this analysis is the ZZ production process. Similarly to the analysis of the $H \to ZZ^{(*)} \to \ell\ell\ell\ell$ channel this background is fully estimated from the Monte Carlo simulation, as are the WW and WZ backgrounds. The Z+jets and top-quark production backgrounds are also taken from the Monte Carlo but with further verifications in data control regions. The W+jets normalization is obtained from a control region. The signal hypothesis is tested by fitting the transverse mass distribution. This variable is most sensitive for high Higgs boson mass hypotheses and is shown in Fig. 2(b) for the high Higgs boson mass search.

- $H \to ZZ \to \ell\ell qq$: This analysis is sensitive for Higgs boson mass hypotheses in the 200 GeV to 600 GeV range and it is separated into a low and a high mass region where the search criteria are independently optimized, the separation occurs at 280 GeV. Given the sizable branching fraction of the Z decaying into a pair of b-quarks ($\sim 15\%$, which is much larger than the fraction of b-quark jets in the background) the analysis is separated into two categories: the *tagged* analysis where the two jets are b-tagged and the *untagged* analysis where at most one of the jets is b-tagged. The dijet system is scaled to set its invariant mass to that of the Z boson in order to improve the mass resolution of the $\ell\ell qq$ system. This channel uses data corresponding to an integrated luminosity of 1.04 fb^{-1} and is described in detail in Ref. [16]. The dominant background in this analysis is the Z+jets production process. Its normalization is measured in the sidebands of the dijet mass distribution. The other backgrounds are estimated with the Monte Carlo simulation and verified with data control samples for the top-quark background. The dilepton-dijet invariant mass is used as the discriminant and its shape is estimated using Monte Carlo simulation both for the signal and the backgrounds. The acceptance of this channel overlaps significantly with that of the $H \to b\bar{b}$ analysis, however as these two channels span different ranges in Higgs boson mass hypotheses they are disjoined. The mass distributions of the $\ell\ell q\bar{q}$ system for events selected in both the *tagged* and the *untagged* categories are shown in Figs. 2(c) and 2(d) respectively.

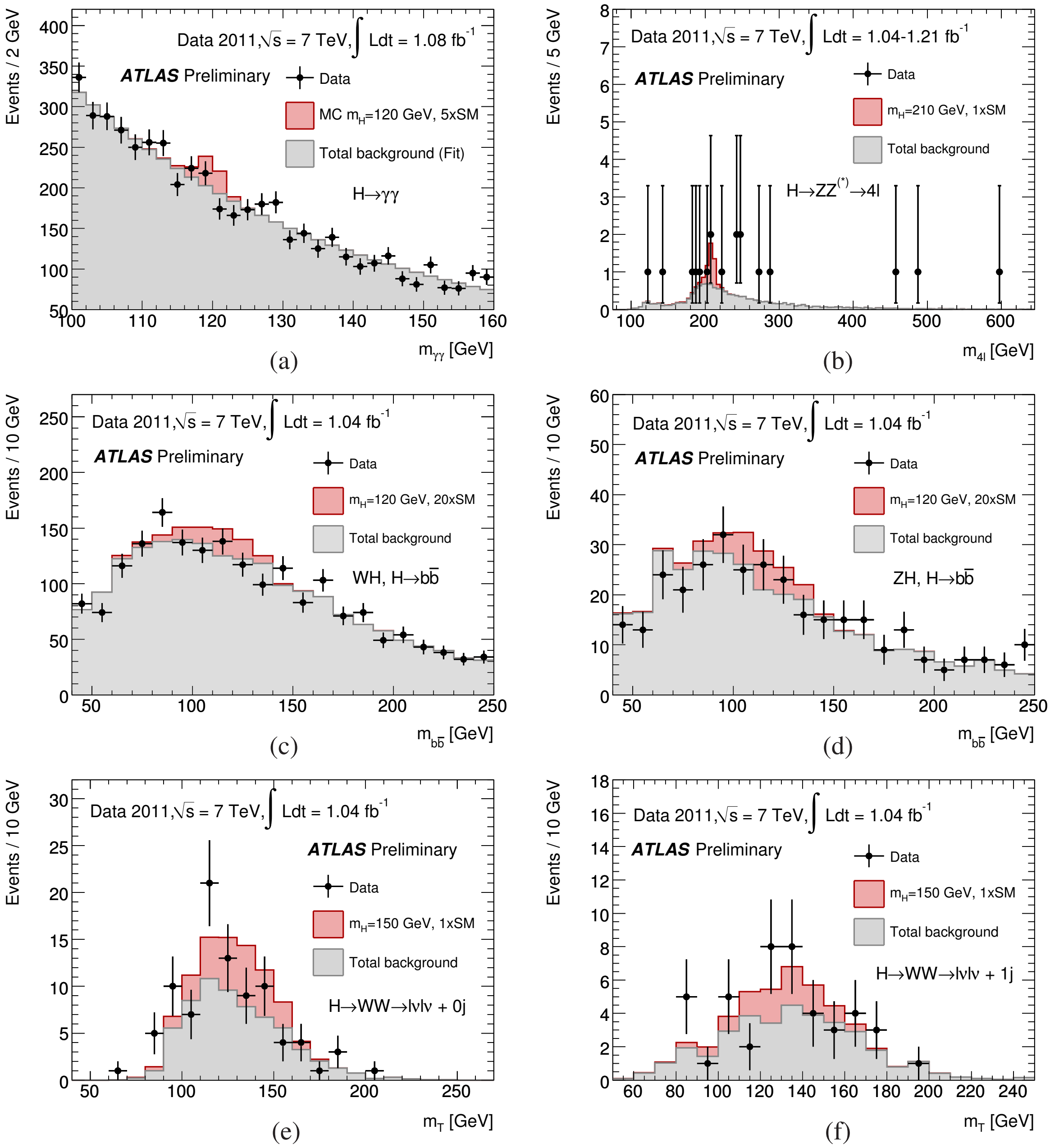

Figure 1: The invariant or transverse mass distributions for the candidate events selected, the total background and the signal expected in the $H \to \gamma\gamma$ (a), $H \to ZZ^{(*)} \to \ell\ell\ell\ell$ (b), the $WH \to \ell\nu b\bar{b}$ (c) and $ZH \to \ell^+\ell^- b\bar{b}$ (d), and the $H \to WW^{(*)} \to \ell\nu\ell\nu$ 0-jet (e) and 1-jet (f) channels. For the $H \to \gamma\gamma$ channel the signal is multiplied by factor of 5 and is illustrated for a Higgs boson mass hypothesis of $m_H = 120$ GeV. For the $H \to ZZ^{(*)} \to \ell\ell\ell\ell$ channel the Higgs boson mass hypothesis is $m_H = 210$ GeV and no multiplicative factor is applied. For the $H \to b\bar{b}$ associated production channels, the Higgs boson mass hypothesis is also $m_H = 120$ GeV, but the multiplicative factor is 20. For the $H \to WW^{(*)} \to \ell\nu\ell\nu$ channels the Higgs boson mass hypothesis is $m_H = 150$ GeV and no multiplicative factor is applied.

Table 1: Numbers of observed events and the expected numbers of signal and background events in the channels used in the combination. For all channels except $H \to WW^{(*)} \to \ell\nu\ell\nu$ these numbers are estimated in an interval containing $\sim 90\%$ of the signal around the most probable value of the invariant or transverse mass distributions. These numbers are for information only as the analyses typically fit the distributions.

	$H \to \gamma\gamma$	$H \to b\bar{b}$	$H \to WW^{(*)}$ $\ell\nu\ell\nu$ 0-jet	$H \to WW^{(*)}$ $\ell\nu\ell\nu$ 1-jet	$H \to WW^{(*)}$ $\ell\nu qq$ 0-jet	$H \to WW^{(*)}$ $\ell\nu qq$ 1-jet	$H \to ZZ^{(*)}$ $\ell\ell\ell\ell$	$H \to ZZ^{(*)}$ $\ell\ell\nu\nu$	$H \to ZZ^{(*)}$ $\ell\ell qq$
m_H=120 GeV									
s	15.9	5.5	2.6	0.9	-	-	0.1	-	-
b	723	992	24.7	7.7	-	-	0.3	-	-
N_{obs}	787	1131	38	9	-	-	0	-	-
m_H=150 GeV									
s	6.9	-	20.5	7.2	-	-	1.1	-	-
b	416	-	32.8	15.2	-	-	0.3	-	-
N_{obs}	405	-	49	21	-	-	1	-	-
m_H=200 GeV									
s	-	-	8.2	3.7	-	-	2.8	4.5	31.4
b	-	-	23.8	19.7	-	-	3.1	62.0	7433
N_{obs}	-	-	19	19	-	-	4	54	7225
m_H=300 GeV									
s	-	-	-	-	19.6	22.0	1.6	9.1	6.8
b	-	-	-	-	3981	3795	2.4	42.3	195
N_{obs}	-	-	-	-	4493	4316	2	38	200
m_H=400 GeV									
s	-	-	-	-	18.8	23.7	1.2	9.0	9.8
b	-	-	-	-	1823	2485	2.2	33.1	207
N_{obs}	-	-	-	-	2005	2790	0	45	239

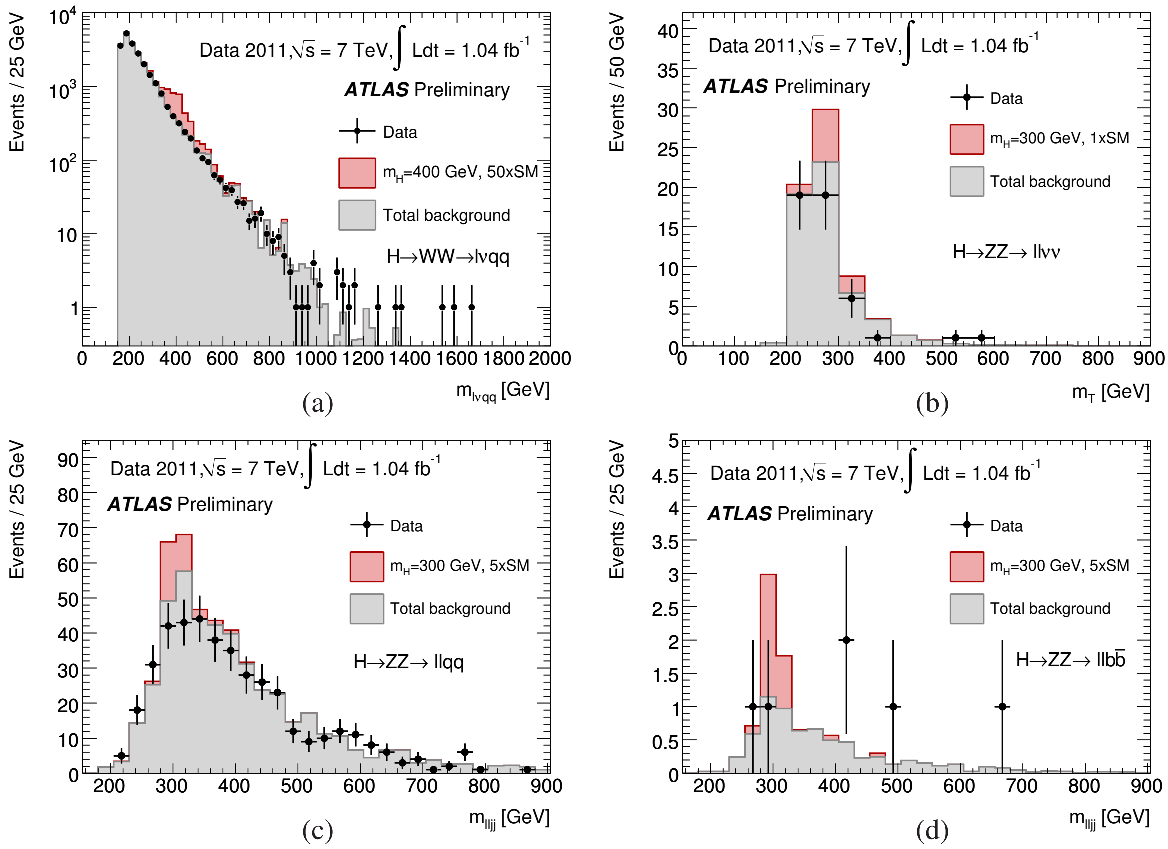

Figure 2: The invariant or transverse mass distributions for the candidate events selected, the total background and the signal expected in the $H \to WW \to \ell\nu qq$ (a) and $H \to ZZ \to \ell\ell\nu\nu$ (b) channels and the $H \to ZZ \to \ell\ell qq$ untagged (c) and tagged (d) categories.

4 Systematic Uncertainties

The combination of Higgs boson search channels is not only useful to optimally take advantage of the full statistical discrimination of the signal from the background in various independent channels, it also allows a proper account to be taken of the correlation of systematic uncertainties between channels. Because all channels rely on a limited number of reconstructed objects in the detector (electrons, photons, muons, jets, missing transverse energy and b-tagging) and on the same Monte Carlo simulation, most of the signal-related systematic uncertainties are correlated. Since in most channels the backgrounds are estimated in control samples of data, the background-related systematic uncertainties are typically uncorrelated. For instance the systematic uncertainty on the luminosity, which is fully correlated among all channels and amounts to $\pm 3.7\%$, affects almost only the signal estimates, except in channels where contributions to the background are directly estimated from Monte Carlo simulation, such as the $H \to ZZ^{(*)}$ modes.

4.1 Detector-related systematic uncertainties

All detector-related systematic uncertainties can be classified in the five generic categories listed below. These categories have been designed to group correlated effects together and thus minimize the number of nuisance parameters in the model. These sources are considered as 100% correlated among channels which are affected by them.

- The electron-related identification systematic uncertainties are treated as fully correlated with those of the photon identification since the selection criteria used are very similar. The partial correlations between the electron energy resolution and energy scale have been neglected.
- The muon momentum scale is precisely known and its attached uncertainty is thus irrelevant in the context of these searches. The systematic uncertainty on the resolution are split in two independent contributions, one due to the inner detector and the other due to the muon system.
- The systematic uncertainty on the jet energy scale (JES) and resolution (JER) may produce significant discrepancies in the jet reconstruction and jet veto efficiencies. The uncertainties have been determined in ATLAS for the 2010 dataset [20, 21]. The effect of the presence of close-by jets and the large additional in-time and out-of-time pile-up in 2011 are also taken into account. For jets at low transverse momentum the JES uncertainties have therefore been increased with respect to those of Ref. [20]. A specific treatment for *b-tagged* jets is applied and considered as fully correlated with the JES.
- The systematic uncertainty on the missing transverse energy has four components. The calorimeter energy scale, the jets, the unclustered energy in the calorimeter and the muon energy scale uncertainty. Its principal component is the JES uncertainty [12, 22], it is therefore treated as correlated with the JES. A systematic uncertainty to account for the large pile-up conditions is added.
- The use of b-tagging requires a thorough understanding of its efficiency and light-flavour mistag rate. The b-tag efficiency is defined as the fraction of reconstructed jets originating from b-quarks which are tagged by the algorithm, whereas the mistag rate is defined as the fraction of jets originating from light-flavoured quarks similarly tagged. The b-tagging efficiencies are estimated using $t\bar{t}$ events with a sample of jets containing muons. Mistag rates are calculated with a sample of inclusive jets, following the procedures described in Ref. [23].

Detector-related sources of systematic uncertainties in the event reconstruction are correlated between all the Higgs boson search channels. The uncertainty in the efficiency ranges between $\pm 2.5\%$ for central high-p_{T} electrons and $\pm 16\%$ for low-p_{T} electrons. For muons the efficiency uncertainty lies between $\pm 0.4\%$ and $\pm 2\%$ depending on their pT and pseudorapidity. The systematic uncertainties are typically larger for the channels where jets are required. They are dominated by the jet energy scale as the resolution affects are smaller and the uncertainties related to the missing transverse energy measurement are largely by-products of the uncertainties already discussed.

4.2 Systematic uncertainties on the theoretical predictions

The Higgs boson production cross sections and decay branching ratios are compiled in Ref. [24]. Higher-order corrections have been calculated up to next-to-next-to-leading order (NNLO) in QCD for the gluon fusion ($gg \to H$) [25–30], vector boson fusion ($qq' \to qq'H$) [31] and associated WH/ZH production processes ($q\bar{q} \to WH/ZH$) [32], and to next-to-leading order (NLO) for the associated production with a $t\bar{t}$ pair ($q\bar{q}/gg \to t\bar{t}H$) [33, 34]. The NLO electroweak (EW) corrections are applied to the gluon fusion [35, 36], vector boson fusion [37, 38] and the associated WH/ZH production [39] processes. The Higgs boson decay branching ratios are calculated with HDECAY [40]. For four-fermion final states the predictions by Prophecy4f [41, 42] are used. The uncertainties in the main Higgs boson production cross section[3] [24, 43] amount to $\pm$(15-20)% for the $gg \to H$ process, $\pm$(3-9)% for the $qq' \to qq'H$ process,

[3]The uncertainties in Higgs boson production cross sections comply with the recommendations of LHC Higgs cross section and PDF4LHC working groups.

$\pm 5\%$ for the associated WH/ZH production process and $\pm(12\text{-}18)\%$ for the $q\bar{q}/gg \to t\bar{t}H$ production process.
For the H$\to$ZZ Monte Carlo samples, the Higgs boson signal is generated using PYTHIA [44] interfaced to PHOTOS [45] for final-state radiation or POWHEG [46]. The $H \to WW^{(*)} \to \ell\nu\ell\nu$ events produced by gluon fusion or vector boson fusion are modelled using the MC@NLO [47, 48] and SHERPA [49] Monte Carlo generators, respectively. The $H \to WW \to \ell\nu qq$ process is modelled by POWHEG [46] and PYTHIA for both the gluon fusion and the vector boson fusion. The $\gamma\gamma$ signal is simulated with POWHEG for the gluon fusion and vector boson fusion processes and with PYTHIA for the associated production processes.

The systematic uncertainty coming from the total theoretical Higgs boson cross section is fully correlated among channels and is included in the combination. The width of the Higgs boson signal at high mass is taken from the POWHEG Monte Carlo. It should be noted that this estimate does not take into account the higher order electroweak corrections that can affect the Higgs boson width at the level of $\pm 30\%$ for very high Higgs boson masses [50].

The uncertainties on the acceptance of the analyses are small in comparison to those on the total cross section and are thus in general neglected. The sole exceptions are the theoretical uncertainties associated to the exclusive production modes where the Higgs boson is associated with additional jets which are sensitive to the choice of the QCD scale. The procedure adopted was recently agreed upon as described in detail in Refs. [12, 51].

A detailed description of the backgrounds used in the analyses is available in Refs. [10–16, 19]. The systematic uncertainties related to the background estimates which rely on the Monte Carlo simulation are taken as fully correlated among channels. The systematic uncertainties arising from the scaling factors that relate the background control regions to the signal regions in analyses such as the $H \to WW^{(*)} \to \ell\nu\ell\nu$, even if estimated using the same Monte Carlo simulation, are not correlated to the systematic uncertainties on the normalization of these backgrounds.

Systematic uncertainties on the signal shape are accounted for in the $H \to \gamma\gamma$, $H \to ZZ \to \ell\ell qq$ and $H \to ZZ \to \ell\ell\nu\nu$ channels. In the $H \to \gamma\gamma$ channel the effect of the uncertainty in the signal shape is estimated by allowing the photon energy resolution to vary and be fitted as an additional nuisance parameter. For all the other channels in the combination it is taken into account by considering three distributions corresponding to the nominal and $\pm 1\sigma$ excursions of the shape and interpolating (extrapolating if necessary) according to the pull of the corresponding nuisance parameter. The systematic uncertainties in the shapes are considered and treated as fully correlated with the systematic uncertainties in the corresponding normalizations. This is in particular the case for the JES or lepton energy scale uncertainties.

The effect on the signal yield in each channel of the major sources of systematic uncertainty is summarised in Table 2. Uncertainties are treated as either uncorrelated or 100% correlated among channels. The correlations between signal and background are also taken into account where necessary.

5 Combined Results

The combination procedure follows closely that described in Refs. [10, 51]. It is based on the profile likelihood technique using the $\tilde{q}_\mu$ test statistic [52]:

$$\tilde{q}_\mu = \begin{cases} -2\ln\frac{\mathscr{L}(\mu,\hat{\hat{\theta}}(\mu))}{\mathscr{L}(0,\hat{\hat{\theta}}(0))}, & \hat{\mu} < 0, \\ -2\ln\frac{\mathscr{L}(\mu,\hat{\hat{\theta}}(\mu))}{\mathscr{L}(\hat{\mu},\hat{\theta})}, & 0 \le \hat{\mu} \le \mu, \\ 0, & \hat{\mu} > \mu. \end{cases}$$

Table 2: Main correlated systematic uncertainties used in the analysis. These relative uncertainties (%) correspond to the overall effect on the per-event signal efficiency of the $\pm 1\sigma$ variation of the source of systematic uncertainty. Some of them, such as the energy scale in the $H \to \gamma\gamma$ search, are included but are not apparent in this table as they do not affect event rates.

	$H \to \gamma\gamma$	$H \to b\bar{b}$	$H \to WW^{(*)}$ $\ell\nu\ell\nu$	$H \to WW^{(*)}$ $\ell\nu qq$	$H \to ZZ^{(*)}$ $\ell\ell\ell\ell$	$H \to ZZ^{(*)}$ $\ell\ell\nu\nu$	$H \to ZZ^{(*)}$ $\ell\ell qq$
Luminosity	± 3.7	± 3.7	± 3.7	± 3.7	± 3.7	± 3.7	± 3.7
e/γ efficiency	$^{+11.6}_{-10.4}$	± 2.3	± 1.4	$^{+0.9}_{-0.8}$	± 1.9	± 1.2	± 1.1
e/γ energy scale	-	$^{+1.5}_{-1.6}$	$^{+0.1}_{-0.4}$	-	-	$^{+0.8}_{-1.1}$	
e/γ resolution	-	$^{+2.1}_{-1.5}$	$^{+0.0}_{-0.5}$	-	-	-	
μ efficiency	-	$^{+1.1}_{-2.0}$	$^{+0.6}_{-0.6}$	± 0.3	± 1.2	$^{+0.8}_{-0.7}$	± 0.6
μ resolution	-	± 5.8	$^{+4.2}_{-4.5}$	-	-	-	
Jet/MET energy scale	-	$^{+21}_{-17}$	$^{+4.6}_{-7.9}$	$^{+15}_{-18}$	-	$^{+5.9}_{-4.0}$	$^{+3.7}_{-10.4}$
Jet resolution	-	± 2.5	-	$^{+8.2}_{-9.0}$	-	-	$^{+2.1}_{-0.0}$
MET	-	$^{+5.5}_{-6.1}$	-	-	-	$^{+6.6}_{-4.2}$	-
b-tag efficiency	-	$^{+37}_{-33}$	-	-	-	$^{+4.3}_{-4.4}$	-
Theory	$^{+15.0}_{-20.0}$	± 5	$^{+15.0}_{-20.0}$	$^{+15.0}_{-20.0}$	$^{+15.0}_{-20.0}$	$^{+15.0}_{-20.0}$	$^{+15.0}_{-20.0}$

The likelihood is given by the product of the individual likelihoods for each channel

$$\mathscr{L} = \prod_l \mathscr{L}_l(N_l^{obs}|N_l^{exp}) \times \prod_i \mathscr{L}_i(\delta_i))$$

where l is implicitly an index over the individual histogram bins within the channels that used a binned distribution of a discriminating variable. The L_i are constrained terms in the likelihood associated to the systematic uncertainties. N_l^{obs} and N_l^{exp} are the observed and expected numbers of events in channel l (this symbolic notation is used for illustration purposes only, in practice analyses based on unbinned likelihood fits are also used in the combination, a more detailed and general description of the method can be found in Ref. [51]). The signal strength μ is the parameter of interest while θ represents the nuisance parameters, such as systematic uncertainties, which can alter the tension between a signal strength hypothesis μ and its best-fit-value. The maximum likelihood estimates or best-fit-values of μ and θ are denoted $\hat{\mu}$ and $\hat{\theta}$, while $\hat{\hat{\theta}}(\mu)$ denotes the conditional maximum likelihood estimate of all nuisance parameters with μ fixed. In this analysis the range of μ is restricted to the physically meaningful regime, *i.e.* it is not allowed to be negative. N_l^{exp} is given by

$$\begin{aligned} N_l^{exp} \quad &= \quad \mu L\, \sigma_l \prod_i (1 + \varepsilon_{li}^{s} \delta_i) + \\ &\quad \sum_j b_{jl} \prod_i (1 + \varepsilon_{j_l i}^{b} \delta_i) \end{aligned} \tag{1}$$

for luminosity L, Standard Model cross sections σ_l (including efficiencies and acceptances), and expected backgrounds b_{jl}. Background estimates b_{jl} may come either from Monte Carlo simulations or from control regions j. Systematic uncertainties are considered either fully or non-correlated and are described by the ε and δ parameters [10]. Monte Carlo pseudo-experiments are generated to construct the probability density functions $f(\tilde{q}_\mu|\mu, \hat{\hat{\theta}}(\mu))$ under an assumed signal strength μ, $f(\tilde{q}_\mu|\mu = 0, \hat{\hat{\theta}}(0))$

and $f(q_0|\mu=0,\hat{\hat{\theta}}(0))$, giving the corresponding p-values, $p_\mu, 1-p_b$ and p_0, from which the $CL_{s+b} = p_\mu, CL_s = \frac{p_\mu}{1-p_b}$ is computed.

The results shown in this note are derived using three different approaches. The first is the asymptotic approximation following the prescriptions given in Ref. [52]. This method has the advantage of reducing immensely the computing time consumption, but needs to be thoroughly validated in order to be applied. The second is the usual Monte Carlo experiments approach where each experiment involves a fit with a very large number of degrees of freedom and therefore requires both a large computing time and a thorough verification of the convergence of the fits. Finally, the third is a Bayesian approach based on the marginalisation of nuisance parameters and fits which assumes a flat prior in strength parameter. It implies less computing time and provides an independent check of the result. The asymptotic limit was found to be reached in most of the Higgs boson mass range, except for very high masses, as described in Appendix A.

The interpretation in terms of limits is then given both using the CL_s method [53] and in the *Power Constrained Limits* [10, 54] (PCL). The former should be taken as the actual result. In contrast to the analysis of Ref. [10], the uncertainties on the cross section are included in the profile likelihood construction.

The 95% CL cross section limits in units of the Standard Model expectation set by the individual channels using the CL_s prescription are shown in Fig. 3. Only the $H \to WW^{(*)} \to \ell\nu\ell\nu$ channel has a median result which is sensitive to the Standard Model Higgs boson, but the $H \to ZZ \to \ell\ell\nu\nu$ excludes a larger mass range. The relative importance of the different channels and whether they bring excesses or deficits is illustrated in this figure.

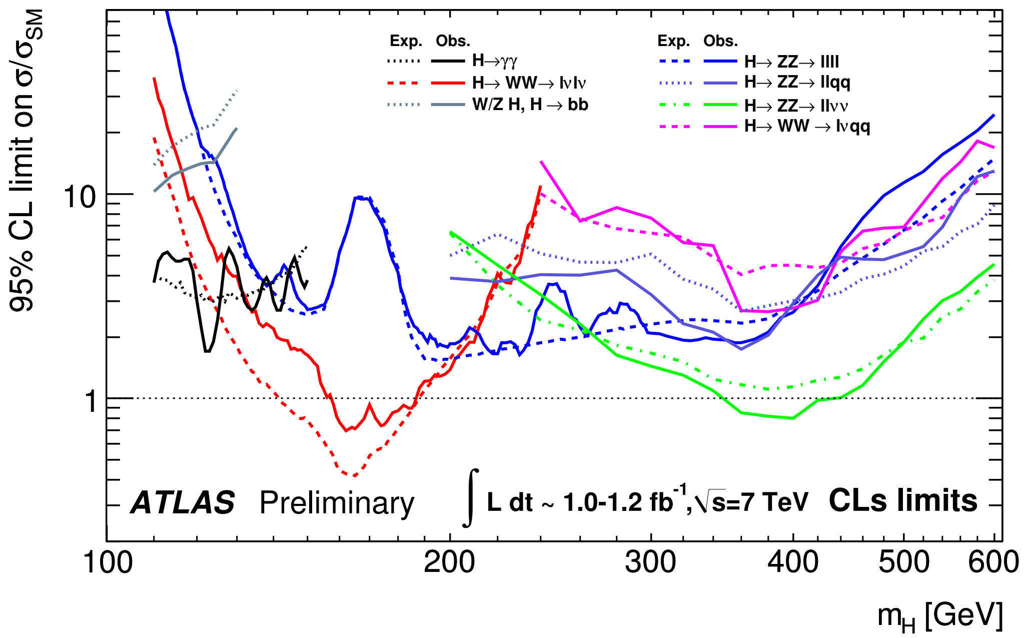

Figure 3: The expected (dashed) and observed (solid) cross-section limits for the individual search channels, normalized to the Standard Model Higgs boson cross section, as functions of the Higgs boson mass. These results use the profile likelihood technique with 95% CL limits using the CL_S construction.

The combination of all channels is shown in Figs. 4(a) and 4(b) in terms of the observed and the expected upper limit at a 95% CL on the excluded Higgs boson production cross section, normalized to the Standard Model value. Full numerical details can be found in Table 6. The limits shown are made using the asymptotic approximation [52] which has been verified using Monte Carlo experiments and a Bayesian calculation which agrees to these results to within a few percent. The median result would exclude a Standard Model Higgs boson in the mass range from 135 GeV to 197 GeV and 315 GeV to 465 GeV. The observed 95% CL exclusion regions are from 155 GeV to 190 GeV and 295 GeV to 450 GeV. A deficit of events is observed in the excluded mass range and in particular in the 300 to 400 GeV mass range. This deficit is not particularly significant ($\sim 2\sigma$) and it is due to the concordance of various small deficits in several high mass channels.

The combined limits derived using the PCL method [54], with a power constraint at 50%, are shown in Figs. 5(a) and 5(b). The PCL interpretation of the combined result gives a limit with exact coverage until the power constraint is invoked, corresponding to the precise 95% Confidence Level obtained from the p-value, $p_\mu = CL_{s+b}$. When a downward fluctuation of the background is observed it is also reflected in the p_μ value, therefore yielding less meaningful limits on the signal. This feature is illustrated in the downward fluctuation, mentioned above, in the 300 to 400 GeV mass range, which would imply a signal exclusion of 0 events. To bound observed limits within the analysis sensitivity domain the power constraint is chosen to be 50%.

The consistency with the background-only hypothesis is computed using the test statistic q_0 from which the probability that a background-only experiment fluctuates more than a given observation can be derived. The value of this test statistic being set to zero if the best-fit-value of the strength parameter is negative, the probability p_0 is bounded to be equal to 50% for downward fluctuations of the background and smaller than 50% when an excess of events is observed. The background fluctuation probability p_0 is displayed as a function of the Higgs boson mass hypothesis in Figs. 6(a) and 6(b). The presence of a signal would give rise to a low value of this compatibility probability. Negative signals ($\hat{\mu} < 0$) are not considered in the calculation, p-values are therefore truncated at 0.5. Some fluctuations are to be expected, given the large number of masses tested. The most extreme value is observed at 144 GeV, where the probability of the observed fluctuation is of the order of 0.3%. The significance of this excess is mostly due to an excess observed in the $H \to WW^{(*)} \to \ell\nu\ell\nu$ channel and one event observed in the $H \to ZZ^{(*)} \to \ell\ell\ell\ell$ channel. The probability of observing such a fluctuation anywhere in the range studied (taking into account the *look-elsewhere effect*) is estimated to be of order 8% following the prescription described in Refs. [51, 55]. Another small excess is observed for Higgs boson mass hypotheses near 128 GeV. This excess is also due to the conjunction of an excess in the $H \to \gamma\gamma$ channel and the $H \to WW^{(*)} \to \ell\nu\ell\nu$ excess. Finally, a less significant excess is observed for Higgs boson mass hypotheses around 245 GeV. This excess is mainly due to the $H \to ZZ^{(*)} \to \ell\ell\ell\ell$ channel, with a slight component from the $H \to ZZ \to \ell\ell\nu\nu$ excess.

The significance with which the Standard Model Higgs boson is excluded is shown in Fig. 7(a) and 7(b). It can be seen that a signal of the Standard Model strength is excluded at very high confidence for 360 GeV, while the strongest exclusion in the region around 160 GeV is about 99%. At an exclusion level of 90% the picture is not very different from the 95% level used herein.

6 Conclusions

The outstanding performance of the LHC in 2011 allows for great sensitivity in the combined ATLAS searches for the Standard Model Higgs boson. The total integrated luminosity accumulated by the end of June of this year has exceeded the objective of the LHC and amounts to about 1.1 fb^{-1} of data collected at $\sqrt{s} = 7$ TeV energy. No significant evidence of a signal has yet been observed, although an excess corresponding to a 2.8σ fluctuation of the background occurs in the Higgs boson mass range between 130 GeV and 150 GeV. The probability for such an excess to arise from background, for the combination of all channels and in the range of Higgs boson mass hypotheses searched for, is estimated to be $\sim 8\%$.

The Standard Model Higgs boson is excluded at 95% CL in an unprecedentedly wide range of Higgs

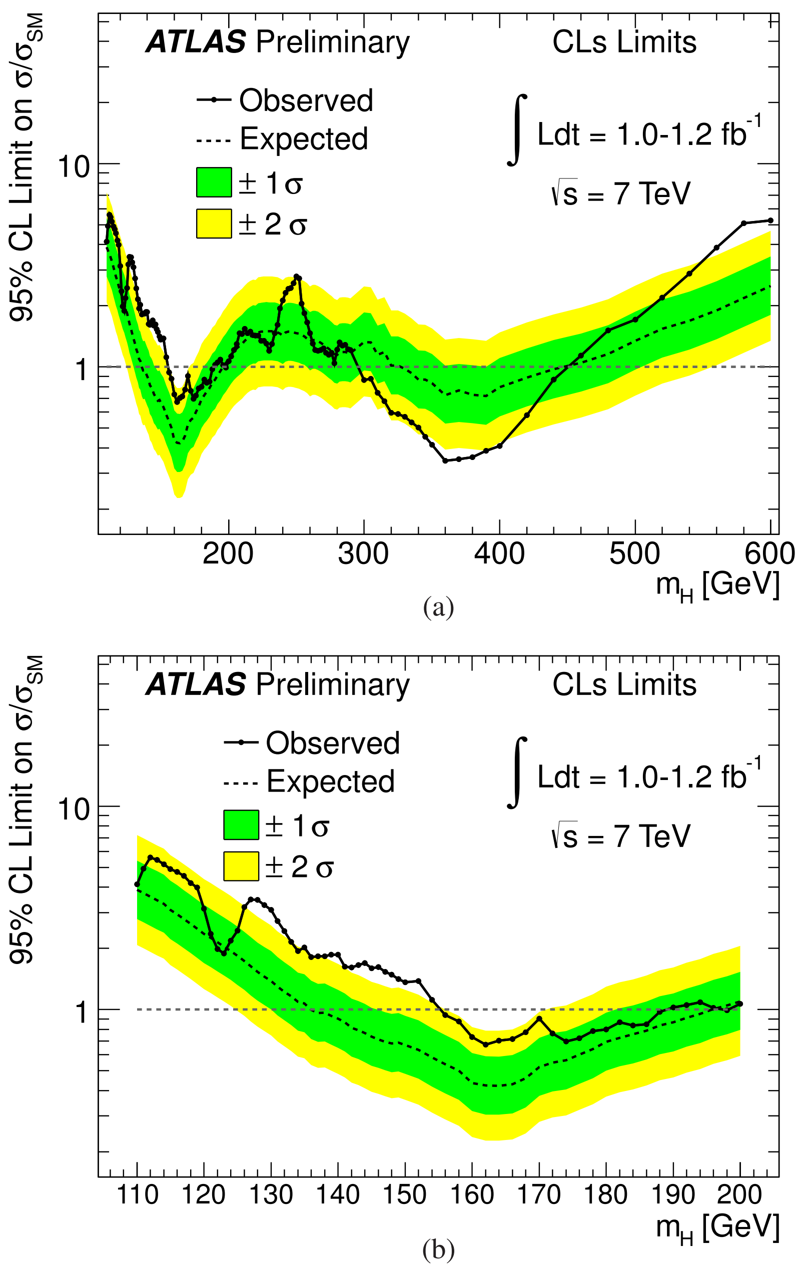

Figure 4: The combined upper limit on the Standard Model Higgs boson production cross section divided by the Standard Model expectation as a function of m_H is indicated by the solid line. This is a 95% CL limit using the CL_s method in the entire mass range (a) and in the low mass range (b). The dotted line shows the median expected limit in the absence of a signal and the green and yellow bands reflect the corresponding 68% and 95% expected regions.

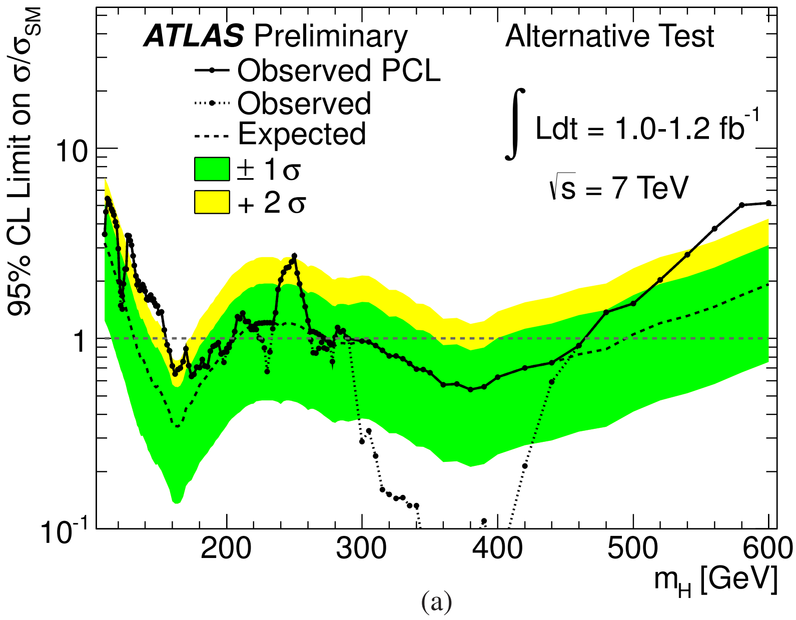

(a)

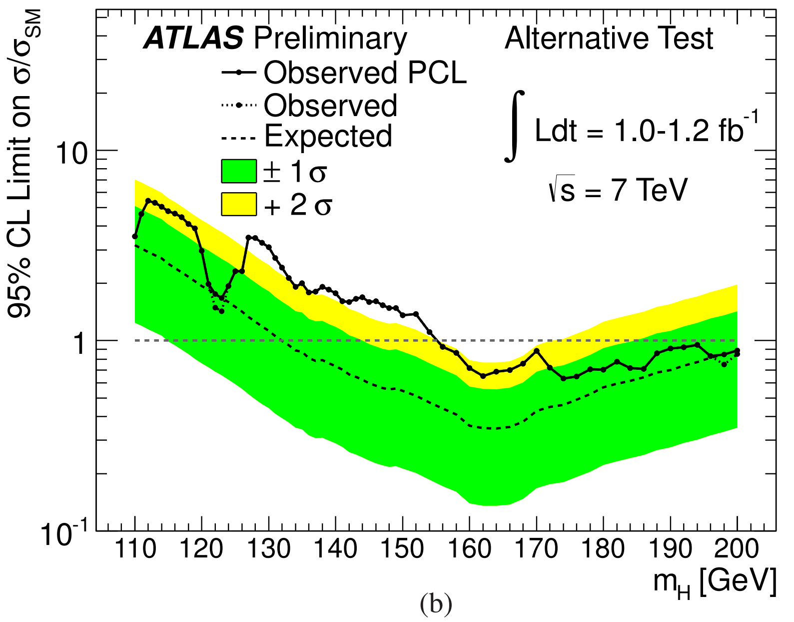

(b)

Figure 5: The combined upper limit on the Standard Model Higgs boson production cross section, normalized to the Standard Model value, as a function of m_H, extracted using the PCL 50% method, is shown in the entire mass range (a) and in the low mass range (b). The dotted line illustrates the observed exclusion obtained from CL_{s+b}, while the solid line illustrates the effect of the power constraint.

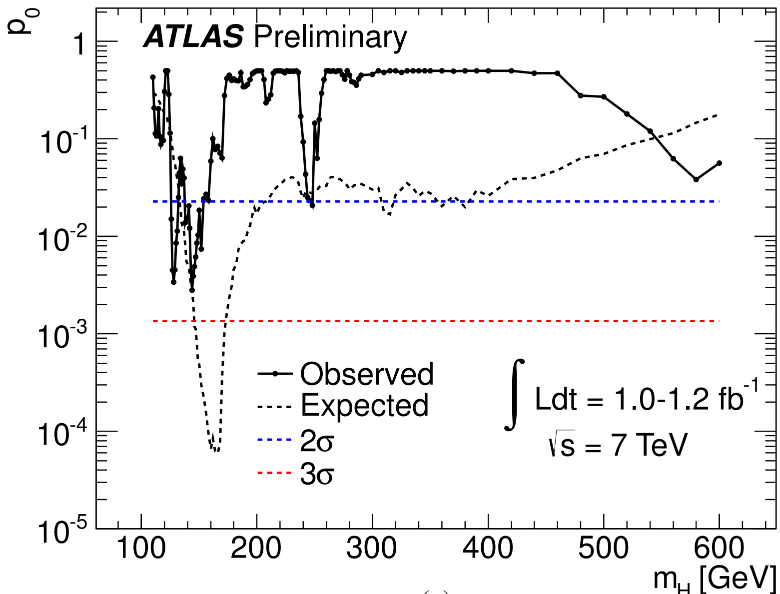

(a)

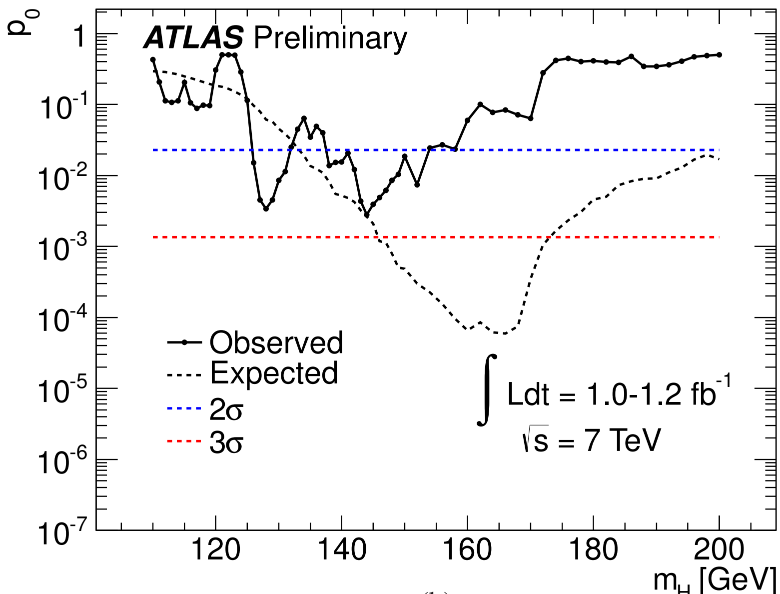

(b)

Figure 6: The consistency of the observed results with the background-only hypothesis is shown in the entire mass range (a) and in the low mass range (b). There are noticeable excesses at 128 GeV and 144 GeV, both receiving a contribution from the excess observed in the $H \to WW^{(*)} \to \ell\nu\ell\nu$ channel. The first one at 128 GeV receives an additional contribution from an excess observed in the $H \to \gamma\gamma$ channel and the second at 145 GeV also receives a contribution from a $H \to ZZ^{(*)} \to \ell\ell\ell\ell$ candidate event. The dashed line shows the median expected significance in the hypothesis of a Standard Model Higgs boson production signal. The two horizontal dashed lines indicate the p-values corresponding to significances of 2σ and 3σ.

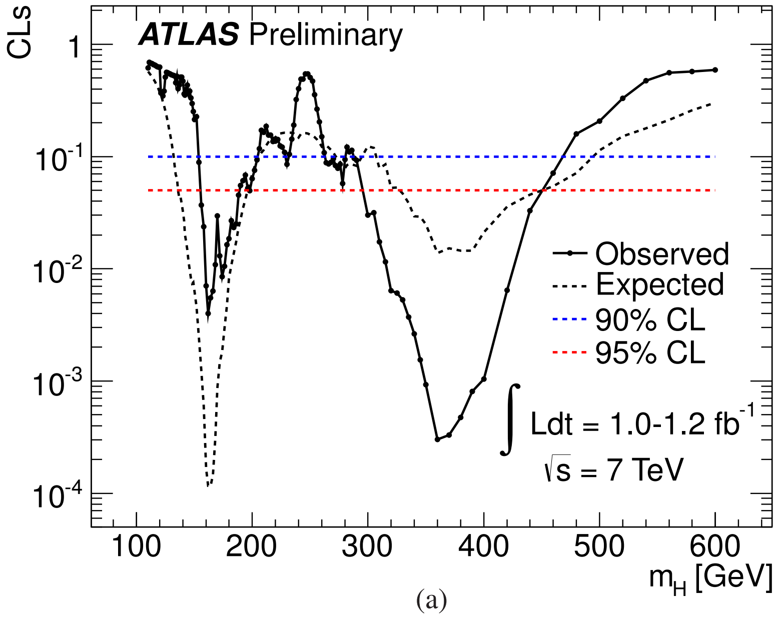

(a)

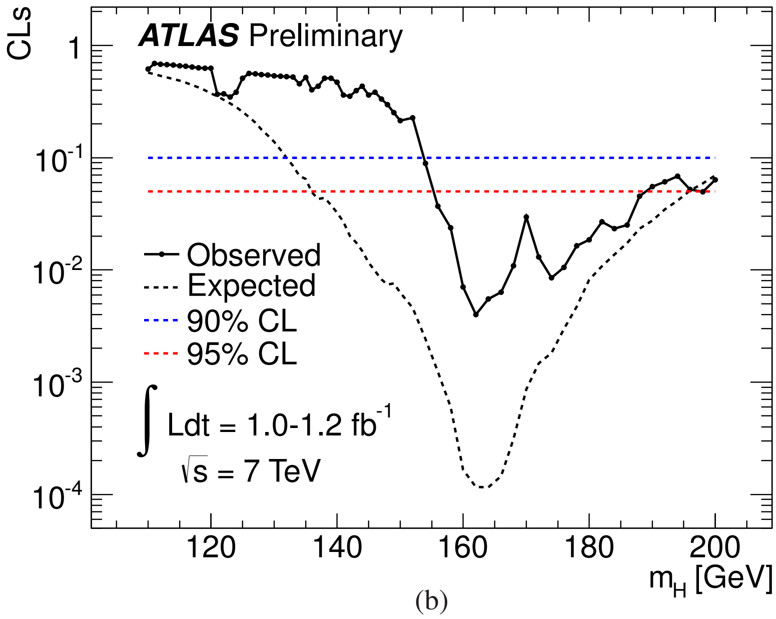

(b)

Figure 7: The value of the combined CL_s for $\mu = 1$ (testing the Standard Model Higgs boson hypothesis) as a function of m_H in the entire mass range (a) and in the low mass range (b). By definition, the regions with $CL_s < \alpha$ are considered excluded at the $(1-\alpha)$ CL or stronger.

boson mass hypotheses in the range from 155 GeV to 190 GeV and 295 GeV to 450 GeV. This is in good agreement with the sensitivity of this search. The excluded region starts to cover a large fraction of the allowed mass range of the Standard Model Higgs boson.

References

[1] F. Englert and R. Brout, *Broken symmetry and the mass of gauge vector mesons*, Phys. Rev. Lett. **13** (1964) 321–323.

[2] P. W. Higgs, *Broken symmetries, massless particles and gauge fields*, Phys. Lett. **12** (1964) 132–133.

[3] P. W. Higgs, *Broken symmetries and the masses of gauge bosons*, Phys. Rev. Lett. **13** (1964) 508–509.

[4] G. Guralnik, C. Hagen, and T. Kibble, *Global conservation laws and massless particles*, Phys. Rev. Lett. **13** (1964) 585–587.

[5] P. W. Higgs, *Spontaneous symmetry breakdown without massless bosons*, Phys. Rev. **145** (1966) 1156–1163.

[6] T. Kibble, *Symmetry breaking in non-Abelian gauge theories*, Phys. Rev. **155** (1967) 1554–1561.

[7] LEP Working Group for Higgs boson searches, *Search for the Standard Model Higgs boson at LEP*, Phys. Lett. **B565** (2003) 61–75.

[8] CDF and D0 Collaborations, *Combined CDF and D0 Upper Limits on Standard Model Higgs Boson Production with up to 8.2 fb^{-1} of Data*, `arXiv:1103.3233 [hep-ex]`.

[9] CDF and D0 Collaborations, *Combined CDF and D0 Upper Limits on Standard Model Higgs-Boson Production with up to 6.7 fb^{-1} of Data*, `arXiv:1007.4587 [hep-ex]`.

[10] ATLAS Collaboration, *Limits on the production of the Standard Model Higgs Boson in pp collisions at $\sqrt{s} = 7$ TeV with the ATLAS detector*, `arXiv:1106.2748 [hep-ex]`.

[11] ATLAS Collaboration, *Search for the Higgs boson in the two photon decay channel with the ATLAS detector at the LHC*, in preparation (2011) .

[12] ATLAS Collaboration, *Search for the Higgs boson in the $H \to WW^{(*)} \to \ell\nu\ell\nu$ decay mode with the ATLAS Detector*, ATLAS-CONF-2011-111 (2011) .

[13] ATLAS Collaboration, *Search for Higgs Boson Production in pp Collisions at $\sqrt{s} = 7$ TeV using the $H \to WW \to \ell\nu qq$ Decay Channel and the ATLAS Detector*, in preparation (2011) .

[14] ATLAS Collaboration, *Search for the Standard Model Higgs boson in the decay channel $H \to ZZ^{(*)} \to \ell\ell\ell\ell$ with 1 fb^{-1} of pp collisions at $\sqrt{s} = 7$ TeV*, in preparation (2011) .

[15] ATLAS Collaboration, *Search for a Standard Model Higgs boson in the mass range 200-600 GeV in the $H \to ZZ \to \ell\ell\nu\nu$ final state with the ATLAS Detector*, in preparation (2011) .

[16] ATLAS Collaboration, *Search for a heavy Standard Model Higgs boson in the channel $H \to ZZ \to \ell\ell qq$ using the ATLAS detector*, in preparation (2011) .

[17] ATLAS Collaboration, *The ATLAS Experiment at the CERN Large Hadron Collider*, JINST **3** (2008) S08003.

[18] J. Campbell, K. Ellis, and C. Williams, *Vector boson pair production at the LHC*, `arXiv:1105.0020 [hep-ph]`.

[19] ATLAS Collaboration, *Search for the Standard Model Higgs boson decaying to a b-quark pair with the ATLAS detector at the LHC*, ATLAS-CONF-2011-103 (2011) .

[20] ATLAS Collaboration, *Jet energy scale and its systematic uncertainty in proton-proton collisions at $\sqrt{s}$=7 TeV in ATLAS 2010 data*, `ATLAS-CONF-2011-032`.

[21] ATLAS Collaboration, *Jet energy resolution and reconstruction efficiencies from in-situ techniques with the ATLAS detector using proton-proton collisions at a center of mass energy $\sqrt{s}$=7 TeV*, `ATLAS-CONF-2010-054`.

[22] ATLAS Collaboration, *Performance of the missing transverse energy reconstruction and calibration in proton-proton collisions at a center-of-mass energy of $\sqrt{s}$=7 TeV with the ATLAS detector*, `ATLAS-CONF-2010-057`.

[23] ATLAS Collaboration, *Commissioning of the ATLAS high-performance b-tagging algorithms in the 7 TeV collision data*, ATLAS-CONF-2011-102 (2011) .

[24] LHC Higgs Cross Section Working Group, S. Dittmaier, C. Mariotti, G. Passarino, and R. Tanaka (Eds.), *Handbook of LHC Higgs cross sections: 1. Inclusive observables*, CERN-2011-002 (CERN, Geneva, 2011) , `arXiv:1101.0593 [hep-ph]`.

[25] R. V. Harlander and W. B. Kilgore, *Next-to-Next-to-Leading Order Higgs Production at Hadron Colliders*, Phys. Rev. Lett. **88** (2002) 201801.

[26] C. Anastasiou and K. Melnikov, *Higgs boson production at hadron colliders in NNLO QCD*, Nucl. Phys. **B646** (2002) 220–256.

[27] V. Ravindran, J. Smith, and W. L. van Neerven, *NNLO corrections to the total cross section for Higgs boson production in hadron hadron collisions*, Nucl. Phys. **B665** (2003) 325–366.

[28] C. Anastasiou, R. Boughezal, and F. Petriello, *Mixed QCD-electroweak corrections to Higgs boson production in gluon fusion*, JHEP **04** (2009) 003.

[29] D. de Florian and M. Grazzini, *Higgs production through gluon fusion: Updated cross sections at the Tevatron and the LHC*, Phys. Lett. **B674** (2009) 291–294.

[30] J. Baglio and A. Djouadi, *Higgs production at the lHC*, JHEP **03** (2011) 055.

[31] P. Bolzoni, F. Maltoni, S.-O. Moch, and M. Zaro, *Higgs Boson Production via Vector-Boson Fusion at Next-to-Next-to-Leading Order in QCD*, Phys. Rev. Lett. **105** (2010) 011801.

[32] O. Brein, A. Djouadi, and R. Harlander, *NNLO QCD corrections to the Higgs-strahlung processes at hadron colliders*, Phys. Lett. **B579** (2004) 149–156.

[33] W. Beenakker et al., *Higgs Radiation Off Top Quarks at the Tevatron and the LHC*, Phys. Rev. Lett. **87** (2001) 201805.

[34] S. Dawson, L. H. Orr, L. Reina, and D. Wackeroth, *Next-to-leading order QCD corrections to $pp \to t\bar{t}h$ at the CERN Large Hadron Collider*, Phys. Rev. **D67** (2003) 071503.

[35] U. Aglietti, R. Bonciani, G. Degrassi, and A. Vicini, *Two-loop light fermion contribution to Higgs production and decays*, Phys. Lett. **B595** (2004) 432–441.

[36] S. Actis, G. Passarino, C. Sturm, and S. Uccirati, *NLO electroweak corrections to Higgs boson production at hadron colliders*, Phys. Lett. **B670** (2008) 12–17.

[37] M. Ciccolini, A. Denner, and S. Dittmaier, *Strong and Electroweak Corrections to the Production of a Higgs Boson+2Jets via Weak Interactions at the Large Hadron Collider*, Phys. Rev. Lett. **99** (2007) 161803.

[38] M. Ciccolini, A. Denner, and S. Dittmaier, *Electroweak and QCD corrections to Higgs production via vector-boson fusion at the LHC*, Phys. Rev. **D77** (2008) 013002.

[39] M. L. Ciccolini, S. Dittmaier, and M. Krämer, *Electroweak radiative corrections to associated WH and ZH production at hadron colliders*, Phys. Rev. **D68** (2003) 073003.

[40] A. Djouadi, J. Kalinowski, and M. Spira, *HDECAY: a program for Higgs boson decays in the Standard Model and its supersymmetric extension*, Comput. Phys. Commun. **108** (1998) 56–74.

[41] A. Bredenstein, A. Denner, S. Dittmaier, and M. M. Weber, *Precise predictions for the Higgs-boson decay $H \to WW/ZZ \to 4$ leptons*, Phys. Rev. **D74** (2006) 013004.

[42] A. Bredenstein, A. Denner, S. Dittmaier, and M. Weber, *Radiative corrections to the semileptonic and hadronic Higgs-boson decays $H \to WW/ZZ \to 4$ fermions*, JHEP **0702** (2007) 080.

[43] M. Botje, J. Butterworth, A. Cooper-Sarkar, A. de Roeck, J. Feltesse, et al., *The PDF4LHC Working Group Interim Recommendations*, `arXiv:1101.0538 [hep-ph]`.

[44] T. Sjostrand, S. Mrenna, and P. Z. Skands, *PYTHIA 6.4 physics and manual*, JHEP **0605** (2006) 026.

[45] P. Golonka and Z. Was, *PHOTOS Monte Carlo: A precision tool for QED corrections in Z and W decays*, Eur. Phys. J. **C45** (2006) 97–107.

[46] P. Nason and C. Oleari, *NLO Higgs boson production via vector-boson fusion matched with shower in POWHEG*, JHEP **02** (2010) 037, `arXiv:0911.5299 [hep-ph]`.

[47] S. Frixione and B. R. Webber, *Matching NLO QCD computations and parton shower simulations*, JHEP **06** (2002) 029.

[48] S. Frixione, P. Nason, and B. R. Webber, *Matching NLO QCD and parton showers in heavy flavour production*, JHEP **08** (2003) 007.

[49] T. Gleisberg et al., *Event generation with SHERPA 1.1*, JHEP **02** (2009) 007, `arXiv:0811.4622 [hep-ph]`.

[50] A. Djouadi, *The anatomy of electro-weak symmetry breaking. I: The Higgs boson in the Standard Model*, Phys. Rept. **457** (2008) 1–216.

[51] ATLAS Collaboration and CMS Collaboration, *LHC Higgs Combination Working Group Report*, ATL-PHYS-PUB-2011-818 (2011) .

[52] G. Cowan, K. Cranmer, E. Gross and O. Vitells, *Asymptotic formulae for likelihood-based tests of new physics*, Eur. Phys. J. **C71** (2011) 1–19.

[53] A. L. Read, *Presentation of search results: The CL(s) technique*, J. Phys. **G28** (2002) 2693–2704.

[54] G. Cowan, K. Cranmer, E. Gross, and O. Vitels, *Power-constrained limits*, `arXiv:1105.3166 [hep-ph]`.

[55] E. Gross and O. Vitells, *Trial factors for the look elsewhere effect in high energy physics*, The European Physical Journal C - Particles and Fields **70** (2010) 525–530.

Appendix A - Comparison of Methods

The asymptotic method used to derive the results shown in this note, following the prescription described in Ref. [52], relies on the assumption of large numbers of events, which is not necessarily the case, even when combining various channels.

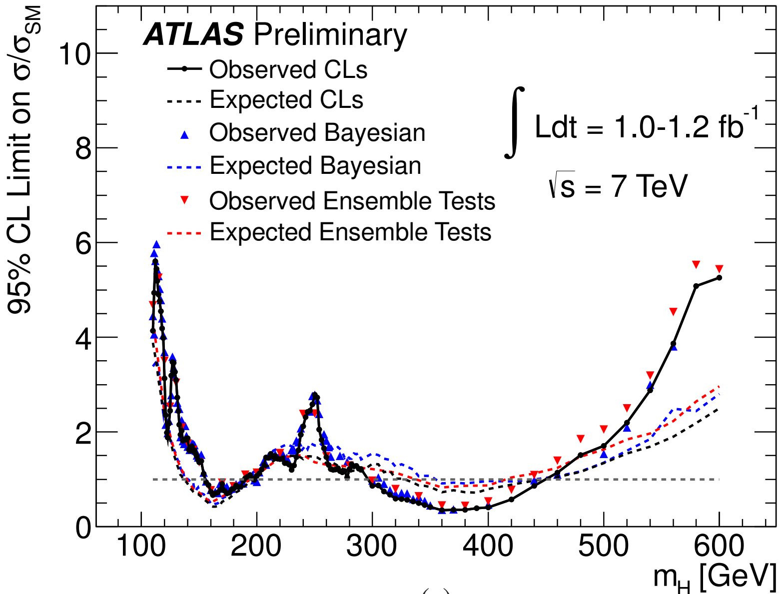

(a)

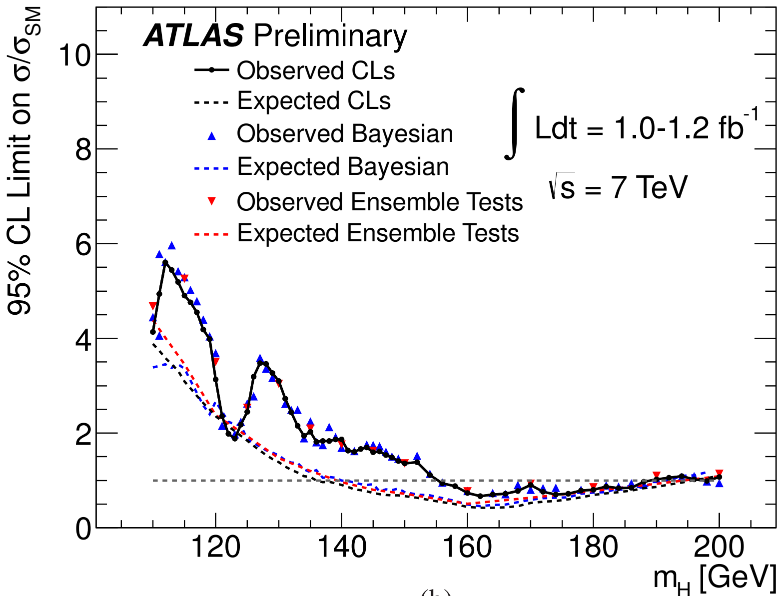

(b)

Figure 8: Comparison of the observed and expected cross section limits for Higgs boson production, normalized to the Standard Model values, estimated using the asymptotic approach, an ensemble of simulated pseudo-experiments and a Bayesian method using a flat prior in signal strength. The comparison is shown over the full mass range (a) and for the low mass range, up to 200 GeV (b).

To validate the use of the asymptotic formulae, limits on the excluded Higgs boson production cross sections, with respect to the Standard Model, were derived with two other methods. The first is the primary method, on which the asymptotic formulae are based, described in Section 5, where limits are estimated using pseudo-experiments. The second is a different approach based on Bayesian confidence intervals assuming a flat prior on the signal strength parameter. A comparison of the results obtained using these two methods and the asymptotic approach is shown in Figs. 8(a) and 8(b). A very good agreement is observed in the low to intermediate mass range. A slight discrepancy is observed in the higher mass range above ~ 300 GeV. It should be noted that the observed Bayesian limit follows very closely the asymptotic limits in this region.

The results on the probability of a background fluctuation p_0 were also derived using asymptotic formulae. These results as well need to be corroborated by pseudo-experiments. As shown in Fig. 9, there is good agreement between $p_0(m_H)$ calculated with pseudo-experiments and the asymptotic expressions used for the primary results over most of the mass range. In the highest mass region, however, the asymptotic expressions are not expected to perform as well due to the very small background and small hypothetical signal rates.

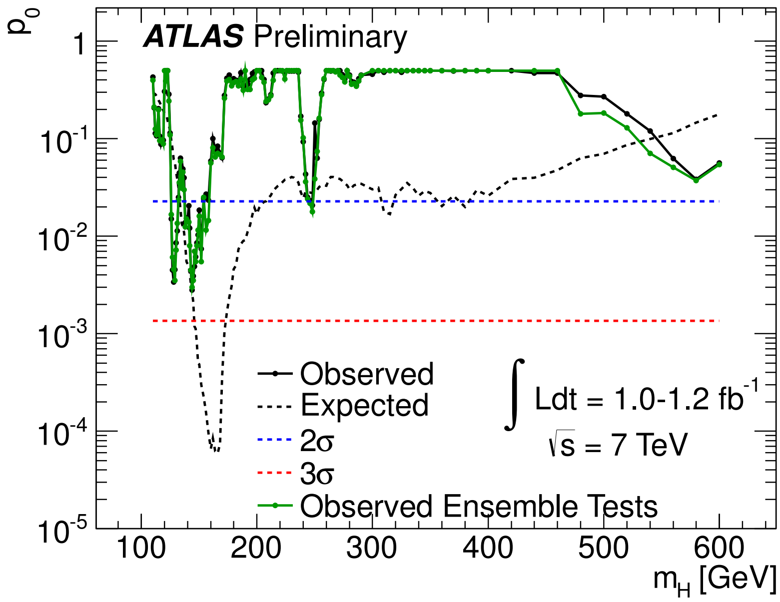

Figure 9: The observed p-value and that expected in the presence of a signal. The results of the asymptotic approach are compared with those obtained using an ensemble of pseudo-experiments.

Appendix B - Results Summary

Table 3: The observed and expected CL_s and PCL limits on the cross sections of a Standard Model Higgs boson production normalized to the Standard Model values for a set of Higgs boson mass hypotheses. The CL_s numbers should be taken as the final result. The p_0-values and $-2\times\ln\frac{\mathscr{L}(1,\hat{\hat{\theta}})}{\mathscr{L}(0,\hat{\hat{\theta}})}$ are also given.

m_H(GeV)	CL_s limits				PCL limits		$-2\times\ln\frac{\mathscr{L}(1,\hat{\hat{\theta}})}{\mathscr{L}(0,\hat{\hat{\theta}})}$	p-values
	Obs.	-1σ	Median	+1σ	Obs.	Median		$p_{\mu=0}$
110	4.2	2.9	4.0	5.5	3.6	3.2	0.1	0.43
111	5.1	2.7	3.8	5.3	4.8	3.1	-0.6	0.21
112	5.8	2.6	3.6	5.1	5.6	3.0	-1.1	0.11
113	5.6	2.5	3.5	4.9	5.4	2.9	-1.2	0.11
114	5.3	2.4	3.4	4.7	5.1	2.7	-1.2	0.11
115	5.0	2.3	3.1	4.4	4.8	2.6	-1.1	0.11
116	4.8	2.1	3.0	4.2	4.7	2.4	-1.2	0.11
117	4.6	2.0	2.8	3.9	4.5	2.3	-1.4	0.089
118	4.2	1.9	2.7	3.7	4.1	2.2	-1.4	0.089
119	4.0	1.8	2.5	3.5	3.9	2.1	-1.5	0.11
120	3.2	1.7	2.4	3.3	3.0	1.9	-0.5	0.22
121	2.4	1.6	2.3	3.1	2.0	1.9	0.7	0.47
122	2.0	1.6	2.1	3.0	1.8	1.8	1.4	0.5
123	1.9	1.5	2.0	2.9	1.7	1.7	1.4	0.49
124	2.2	1.4	1.9	2.7	2.0	1.6	0.1	0.38
125	2.5	1.3	1.8	2.6	2.4	1.5	-1.4	0.11
126	3.2	1.3	1.7	2.4	3.2	1.4	-4.0	0.015
127	3.5	1.2	1.6	2.3	3.5	1.3	-5.3	0.0045
128	3.5	1.1	1.5	2.1	3.5	1.3	-5.7	0.0034
129	3.3	1.1	1.5	2.0	3.3	1.2	-5.5	0.0044
130	3.1	1.0	1.4	1.9	3.1	1.1	-5.4	0.0051
131	2.8	0.9	1.3	1.8	2.8	1.1	-4.7	0.011
132	2.5	0.9	1.2	1.7	2.5	1.0	-4.0	0.025
133	2.2	0.8	1.2	1.6	2.1	1.0	-3.2	0.045
134	2.0	0.8	1.1	1.5	1.9	0.9	-2.6	0.064
135	2.0	0.8	1.1	1.5	2.0	0.9	-3.3	0.035
136	1.8	0.7	1.0	1.4	1.8	0.8	-2.6	0.049
137	1.9	0.7	1.0	1.4	1.8	0.8	-3.3	0.04
138	2.0	0.7	1.0	1.4	2.0	0.8	-4.4	0.014
139	1.9	0.7	0.9	1.3	1.9	0.8	-4.7	0.015
140	1.8	0.7	0.9	1.3	1.8	0.7	-4.6	0.012
141	1.6	0.6	0.9	1.2	1.6	0.7	-4.0	0.021
142	1.6	0.6	0.8	1.1	1.6	0.7	-5.2	0.012
143	1.7	0.6	0.8	1.1	1.7	0.6	-6.8	0.0044
144	1.7	0.6	0.8	1.1	1.7	0.6	-7.9	0.0028

Table 4: The observed and expected CL_s and PCL limits on the cross sections of a Standard Model Higgs boson production normalized to the Standard Model values for a set of Higgs boson mass hypotheses. The CL_s numbers should be taken as the final result. The p_0-values and $-2\times\ln\frac{\mathscr{L}(1,\hat{\hat{\theta}})}{\mathscr{L}(0,\hat{\hat{\theta}})}$ are also given.

m_H(GeV)	CL_s limits				PCL limits		$-2\times\ln\frac{\mathscr{L}(1,\hat{\hat{\theta}})}{\mathscr{L}(0,\hat{\hat{\theta}})}$	p-values
	Obs.	-1σ	Median	+1σ	Obs.	Median		$p_{\mu=0}$
145	1.6	0.5	0.7	1.0	1.6	0.6	-6.9	0.0045
146	1.6	0.5	0.7	1.0	1.6	0.6	-6.9	0.0049
147	1.6	0.5	0.7	1.0	1.6	0.6	-6.1	0.0062
148	1.5	0.5	0.7	1.0	1.5	0.6	-5.4	0.0086
149	1.4	0.5	0.7	1.0	1.4	0.6	-4.4	0.01
150	1.4	0.5	0.7	0.9	1.4	0.5	-3.8	0.019
152	1.4	0.5	0.6	0.9	1.4	0.5	-4.8	0.0074
154	1.1	0.4	0.6	0.8	1.1	0.5	-2.0	0.024
156	0.9	0.4	0.5	0.7	0.9	0.4	0.5	0.027
158	0.9	0.4	0.5	0.7	0.9	0.4	1.0	0.023
160	0.7	0.3	0.4	0.6	0.7	0.4	3.8	0.059
162	0.7	0.3	0.4	0.6	0.7	0.3	5.7	0.1
164	0.7	0.3	0.4	0.6	0.7	0.3	4.7	0.078
166	0.7	0.3	0.4	0.6	0.7	0.4	4.3	0.084
168	0.8	0.3	0.5	0.6	0.8	0.4	3.0	0.072
170	0.9	0.4	0.5	0.7	0.9	0.4	1.4	0.064
172	0.8	0.4	0.5	0.8	0.7	0.4	4.6	0.28
174	0.7	0.4	0.6	0.8	0.6	0.5	6.1	0.42
176	0.7	0.4	0.6	0.8	0.6	0.5	5.8	0.45
178	0.8	0.5	0.6	0.9	0.7	0.5	5.0	0.4
180	0.8	0.5	0.7	1.0	0.7	0.6	5.0	0.41
182	0.9	0.5	0.7	1.0	0.8	0.6	4.3	0.4
184	0.8	0.5	0.8	1.1	0.7	0.6	4.7	0.39
186	0.8	0.6	0.8	1.1	0.7	0.6	4.7	0.47
188	1.0	0.6	0.8	1.2	0.9	0.7	3.4	0.34
190	1.0	0.6	0.9	1.2	0.9	0.7	3.1	0.34
192	1.1	0.7	0.9	1.3	0.9	0.7	3.0	0.36
194	1.1	0.7	1.0	1.3	1.0	0.8	2.8	0.4
196	1.0	0.7	1.0	1.4	0.8	0.8	3.7	0.47
198	1.0	0.8	1.1	1.5	0.8	0.8	4.1	0.49
200	1.1	0.8	1.1	1.5	0.9	0.9	3.5	0.5
202	1.1	0.8	1.1	1.6	0.9	0.9	3.2	0.5
204	1.2	0.9	1.2	1.7	1.0	1.0	2.8	0.5
206	1.3	0.9	1.2	1.7	1.1	1.0	2.3	0.41
208	1.5	0.9	1.3	1.8	1.3	1.0	1.0	0.23
210	1.4	0.9	1.3	1.8	1.3	1.1	1.2	0.26
212	1.5	1.0	1.3	1.9	1.4	1.1	1.1	0.28
214	1.5	1.0	1.4	1.9	1.2	1.1	1.9	0.47

Table 5: The observed and expected CL_s and PCL limits on the cross sections of a Standard Model Higgs boson production normalized to the Standard Model values for a set of Higgs boson mass hypotheses. The CL_s numbers should be taken as the final result. The p_0-values and $-2 \times \ln \frac{\mathscr{L}(1,\hat{\hat{\theta}})}{\mathscr{L}(0,\hat{\hat{\theta}})}$ are also given.

m_H(GeV)	CL_s limits				PCL limits		$-2 \times \ln \frac{\mathscr{L}(1,\hat{\hat{\theta}})}{\mathscr{L}(0,\hat{\hat{\theta}})}$	p-values
	Obs.	-1σ	Median	+1σ	Obs.	Median		$p_{\mu=0}$
216	1.5	1.0	1.4	2.0	1.2	1.1	1.9	0.5
218	1.4	1.0	1.4	2.0	1.2	1.2	2.3	0.5
220	1.4	1.0	1.4	2.0	1.2	1.2	2.3	0.5
222	1.4	1.1	1.5	2.1	1.2	1.2	2.3	0.49
224	1.4	1.1	1.5	2.1	1.2	1.2	2.6	0.47
226	1.3	1.1	1.5	2.1	1.2	1.2	2.7	0.5
228	1.3	1.1	1.5	2.1	1.2	1.2	3.0	0.49
230	1.2	1.1	1.5	2.1	1.2	1.2	3.6	0.49
232	1.3	1.1	1.5	2.1	1.2	1.2	3.1	0.5
234	1.5	1.1	1.5	2.1	1.2	1.2	2.3	0.5
236	1.6	1.1	1.5	2.1	1.4	1.2	1.5	0.48
238	1.9	1.1	1.5	2.0	1.8	1.2	-0.4	0.17
240	2.1	1.0	1.4	2.0	2.0	1.1	-1.6	0.093
242	2.3	1.1	1.5	2.0	2.2	1.2	-2.9	0.043
244	2.4	1.1	1.5	2.1	2.4	1.2	-3.8	0.025
246	2.4	1.1	1.5	2.1	2.4	1.2	-4.0	0.023
248	2.6	1.1	1.5	2.1	2.5	1.2	-4.1	0.021
250	2.8	1.1	1.5	2.0	2.7	1.2	-3.0	0.14
252	2.7	1.1	1.5	2.0	2.2	1.2	-2.3	0.063
254	2.0	1.0	1.4	2.0	1.9	1.2	-0.7	0.16
256	1.8	1.0	1.4	2.0	1.7	1.1	0.5	0.29
258	1.6	1.0	1.4	1.9	1.5	1.1	1.2	0.41
260	1.5	1.0	1.3	1.9	1.2	1.1	1.9	0.5
262	1.3	1.0	1.4	1.9	1.1	1.1	2.7	0.5
264	1.2	1.0	1.4	1.9	1.1	1.1	3.2	0.49
266	1.2	1.0	1.3	1.9	1.1	1.1	3.3	0.5
268	1.2	0.9	1.3	1.8	1.1	1.1	3.1	0.49
270	1.2	0.9	1.3	1.8	1.0	1.0	2.9	0.5
272	1.2	0.9	1.3	1.8	1.0	1.0	3.2	0.5
274	1.1	0.9	1.2	1.7	1.0	1.0	3.3	0.46
276	1.2	0.9	1.2	1.7	1.0	1.0	2.9	0.41
278	1.0	0.8	1.2	1.6	0.9	0.9	3.9	0.5
280	1.2	0.8	1.1	1.6	1.0	0.9	2.6	0.45
282	1.3	0.8	1.2	1.6	1.1	0.9	2.0	0.39
284	1.3	0.9	1.2	1.6	1.1	0.9	2.2	0.38
286	1.3	0.9	1.2	1.6	1.1	0.9	2.1	0.36
288	1.2	0.8	1.2	1.6	1.0	0.9	2.6	0.41
290	1.2	0.8	1.2	1.6	1.0	0.9	2.7	0.45

Table 6: The observed and expected CL_s and PCL limits on the cross sections of a Standard Model Higgs boson production normalized to the Standard Model values for a set of Higgs boson mass hypotheses. The CL_s numbers should be taken as the final result. The p_0-values and $-2\times\ln\frac{\mathscr{L}(1,\hat{\hat{\theta}})}{\mathscr{L}(0,\hat{\hat{\theta}})}$ are also given.

m_H(GeV)	CL_s limits				PCL limits		$-2\times\ln\frac{\mathscr{L}(1,\hat{\hat{\theta}})}{\mathscr{L}(0,\hat{\hat{\theta}})}$	p-values
	Obs.	-1σ	Median	+1σ	Obs.	Median		$p_{\mu=0}$
300	0.9	1.0	1.3	1.9	1.0	1.0	5.8	0.46
305	0.9	1.0	1.3	1.8	1.0	1.0	5.7	0.5
310	0.7	0.8	1.1	1.6	0.9	0.9	6.7	0.48
315	0.7	0.9	1.2	1.6	0.9	0.9	7.8	0.5
320	0.6	0.7	1.0	1.4	0.8	0.8	8.7	0.5
325	0.6	0.7	1.0	1.4	0.8	0.8	8.8	0.48
330	0.6	0.7	1.0	1.4	0.8	0.8	9.1	0.5
335	0.5	0.7	0.9	1.3	0.7	0.7	9.8	0.5
340	0.5	0.6	0.9	1.2	0.7	0.7	10.4	0.5
345	0.5	0.6	0.9	1.2	0.7	0.7	11.6	0.5
350	0.4	0.6	0.8	1.2	0.7	0.7	12.6	0.5
360	0.3	0.5	0.7	1.0	0.6	0.6	14.8	0.5
370	0.4	0.5	0.8	1.0	0.6	0.6	14.6	0.49
380	0.4	0.5	0.7	1.0	0.5	0.5	13.9	0.5
390	0.4	0.5	0.7	1.0	0.6	0.6	12.6	0.5
400	0.4	0.6	0.8	1.1	0.6	0.6	12.3	0.5
420	0.6	0.6	0.9	1.2	0.7	0.7	8.5	0.5
440	0.9	0.7	1.0	1.4	0.7	0.7	4.8	0.47
460	1.1	0.8	1.1	1.5	0.9	0.8	3.0	0.47
480	1.5	0.8	1.2	1.6	1.4	0.9	1.1	0.28
500	1.7	1.0	1.3	1.9	1.5	1.1	0.7	0.27
520	2.2	1.1	1.5	2.1	2.0	1.2	-0.4	0.18
540	2.9	1.2	1.7	2.4	2.8	1.3	-1.3	0.12
560	3.9	1.4	1.9	2.6	3.8	1.5	-2.3	0.063
580	5.1	1.6	2.2	3.0	5.0	1.7	-2.8	0.038
600	5.3	1.8	2.5	3.5	5.2	1.9	-2.2	0.057